RSC Advances

ROYAL SOCIETY OF CHEMISTRY

www.rsc.org/advances

A table of contents entry.

Colour graphic:

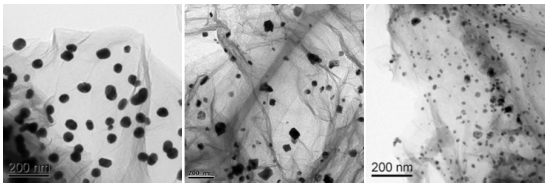

Text:

GO/noble metal (Au, Pt, and Pd) NP composites were synthesized and the corresponding NLO and optical OL properties were investigated.

Cite this: DOI: 10.1039/c0xx00000x

www.rsc.org/xxxxxx

ARTICLE TYPE

Graphene oxide–noble metal (Au, Pt, and Pd) nanoparticle composites as optical limiters

Chan Zheng,*[a] Wenzhe Chen,[a] Huang Yanyi,[a] Xueqing Xiao,[a] and Xiaoyun Ye[a]

Received (in XXX, XXX) Xth XXXXXXXXX 20XX, Accepted Xth XXXXXXXXX 20XX

DOI: 10.1039/b000000x

A series of graphene oxide (GO)/noble metal (Au, Pt, and Pd) nanoparticle (NP) composites were synthesized via a one-step hydrothermal reaction of $HAuCl_4$, H_2PtCl_6, and $Pd(C_2H_3O_2)_2$ in the presence of GO. The metal NPs with different average sizes and distributions were uniformly deposited onto the GO surface. The GO structure was conserved after loading with Au, Pt, and Pd NPs. The corresponding nonlinear optical (NLO) and optical limiting (OL) properties were investigated using an open-aperture Z-scan technique with nanosecond pulses at 532 nm. Results show that the NLO and OL properties were significantly enhanced after the inclusion of metal NPs onto the GO surface because of nonlinear scattering (NLS) effects. These enhancements depend on the type of the loading metal NPs. The GO/Au-NP composite exhibits the optimal NLO and OL performances among the studied composites because of the surface plasmon resonance of Au NPs. Thus, the NLO and OL effects of the two-dimensional GO can be effectively modified by absorbing different metal NPs on its surface. The synthetic NLO and OL properties in the GO/metal NP composites originate from the reverse saturable absorption in the GO sheets and the NLS in metal NPs. All of the results indicate that these composites can be used in optoelectronic applications.

1. Introduction

Lasers have been widely used in medical, measurement, chemical, and military applications, as well as in material processing and preparation, since their introduction in 1960. With the emergence of high-energy and short-pulse laser, optical instruments, particularly the human eyes, can be damaged easily by unexpected irradiation [1–3]. Thus, a significant attention has been focused on the development of "optical limiter" that exhibits high transmittance for low-intensity light and attenuates intense optical beams. Optical limiters can be used to protect optical sensors, such as eyes or charge-coupled device cameras, from the possible damage caused by intense laser pulses and they can be applied in various fields, such as optical switching.

Graphene, a monolayer of carbon atoms packed into a dense honeycomb crystal structure, has gained significant attention because of its excellent electronic, mechanical, optical, and thermal properties derived from its unique two-dimensional structure [4–6]. Such remarkable properties render graphene as a promising material for various applications. The nonlinear optical (NLO) and optical limiting (OL) properties of graphene have also attracted research interests; these properties are due to the extended π-conjugate system and the linear dispersion relation holding for the electronic band structure of graphene [7–12]. Furthermore, graphene presents strong NLO and OL properties, and thus, it can be used as broad-band limiters. The excellent OL properties of graphene mainly originate from nonlinear scattering (NLS), reverse saturable absorption (RSA), two-photon absorption (TPA), and multi-photon absorption differ from materials and laser pulses [7–12].

In addition, graphene is an ideal substrate in synthesizing and designing multicomponent materials because of its large 2D aromatic surface and the presence of oxygen groups, such as hydroxyls and epoxides, on its surface; these oxygen groups can provide reactive sites for chemical modification using a recognized carbon surface chemistry [13–15]. The present results indicate that nanocomposites based on graphene and its derivatives, including covalently or noncovalently functionalized graphene composites, show improved NLO or OL properties compared with pure graphene; multifunctional composite materials exhibit the superior properties of graphene and a functionalizing material, and thus, various studies have explored the possibility of using graphene-based composites as optical limiters [16–20]. For example, Zhu et al. [16] reported that graphene oxide (GO) covalently functionalized with zinc phthalocyanine exhibits higher NLO extinction coefficients and broadband OL performance than GO at 532 and 1064 nm. Feng et al. [17] fabricated CdS noncovalently functionalized in graphene nanosheets (GNS–CdS) and found that the GNS–CdS composites suspended in dimethylformaminde exhibit optimum OL properties.

Noble metal nanoparticles (NPs), such as Au and Ag, possess significant NLO properties and ultra-fast response times. Their optical properties have been extensively investigated with the use of picosecond and femtosecond lasers on the surface plasmon resonance (SPR) region [21–23]. The combination of the NLO performances of graphene and metal NPs can provide exceptional and unique behavior, which should be further investigated. In a previous study [18], the NLO and OL properties of graphene composites with Pt and Pd NPs were investigated; and the SPRs of these composites are generally found at the UV region, which are far away from the laser excitations. Moreover, the NLO and OL properties of graphene with Au or Ag NPs are rarely reported.

In the present study, Au, Pt, and Pd NPs were homogeneously deposited onto the surface of GO sheets. Transmission electron

microscopy (TEM), X-ray photo-electron spectroscopy (XPS), and Raman spectroscopy were used to elucidate the surface morphology and structure of GO/metal NPs. Au, Pt, and Pd coated with GO demonstrate significant NLO and OL properties compared with pure GO. The enhanced mechanisms were also discussed.

2. Experimental

2.1 Synthesis of GO/metal NPs

2.1.1 Synthesis of GO

Graphene was prepared by oxidizing natural graphite powder via modified Hummers' method [24]. Approximately 10 g of graphite powder and 5 g of sodium nitrate were simultaneously stirred in concentrated sulfuric acid (230 mL) and cooled in an ice bath. Subsequently, 30 g of potassium permanganate was gradually added to produce a new mixture. The mixture was allowed to warm to room temperature and then heated to 35 ℃ in a water bath. The mixture was gently stirred for 2 h. The reaction mixture was cooled in an ice bath, and distilled water was added in excess to the mixture. After adding aqueous hydrogen peroxide solution (30 wt%), the mixture was stirred for 2 h to reduce excess $KMnO_4$. The resultant suspension was intensively washed with diluted HCl solution and then with distilled water via filtration. Subsequently, the suspension was centrifuged at 3000 rpm to remove the residual unexfoliated graphite and oxidative agents. The resulting material was dried through lyophilization to obtain the GO powder.

2.1.2 Synthesis of GO/Au-NPs

Aqueous GO suspension (30 mL) was added to 20 mL of $HAuCl_4$ solution (2.5 mM), and the solution was boiled at 100 ℃. Sodium citrate (0.04 M, 5 mL) was added to the boiling solution and then subsequently refluxed for 30 min. The obtained nanocomposite was washed with distilled water and centrifuged (3000 rpm) to remove the free Au NPs formed in the solution. The final nanocomposite was dried through lyophilization.

2.1.3 Synthesis of GO/Pt-NPs

Approximately 30 mL of GO was dispersed into 45 mL of H_2PtCl_6 aqueous solution (4.0 mM) through ultrasonication. The solution was boiled at 100 ℃. Sodium citrate (0.08 M, 10 mL) was added to the boiling solution, which was then refluxed for 30 min. The resultant nanocomposite was washed with distilled water and centrifuged (3000 rpm) to remove the free Pt NPs formed in the solution. The final nanocomposite was dried through lyophilization.

2.1.4 Synthesis of GO/Pd-NPs

Approximately 30 mL of GO was dispersed in 45 mL aqueous graphene suspension through ultrasonication. Sodium citrate (0.27 g) was added to the suspension, which was then boiled at 100 ℃. Subsequently, 8.6 mg of palladium acetate and 2.3 mL ascorbic acid solution (0.1 mol L^{-1}) were successively and rapidly added to the system. The solution was then refluxed for 2.5 h. The obtained nanocomposite was washed with distilled water and centrifuged (3000 rpm) to remove the free Pd NPs formed in the solution. The final nanocomposite was dried through lyophilization.

2.2 Characterization

The morphology of the obtained GO/metal NPs was investigated using TEM (JEM-2010; accelerating voltage, 200 kV). The samples were ultrasonicated in ethanol to ensure dispersion. A drop of the dispersed sample was left to dry on a commercial carbon-coated Cu TEM grid. XPS was performed with the use of an Escalab 250 (ThermoFisher Scientific CO.) with Al Kα as the excitation source. Binding energies were corrected with the C1s peak at 285 eV when the samples exhibited mild charging. The Raman spectra of the GO and GO/metal NP composites were obtained using a Raman spectrometer (Renishaw Invia) at ambient temperature and 785 nm excitation wavelength.

2.3 Z-scan measurement

The NLO and OL behavior of the GO and GO/metal NPs was evaluated through open-aperture (OA) *Z*-scan technique [25]. The excitation light source was an Nd:YAG laser (Brio 640, Quantel, Les Ulis, France) with a repetition rate of 1 Hz. The laser pulses (period, 4 ns; wavelength, 532 nm) were split into two beams with a mirror. The pulse energies in the front and back of the samples were monitored using D1 and D2 energy detectors (PE25, Ophir Optronics Solutions Ltd., Jerusalem, Israel). The laser beam waist was approximately 14.5 μm, whereas the energy of a single pulse was set at 200 μJ. All of the measurements were conducted at room temperature. The sample was dispersed in ethanol and put into 1 mm-thick glass cuvettes. Each sample was mounted on a computer-controlled translation stage that shifts the sample along the *z*-axis.

3. Results and discussion

3.1 Morphology of the GO/metal NP composites

The GO/metal NP composites were synthesized via a one-step hydrothermal reaction of $HAuCl_4$, H_2PtCl_6, and $Pd(C_2H_3O_2)_2$ in the presence of GO. During synthesis, the oxygen-functional groups, such as epoxy, hydroxyl, and carboxyl, in the GO surfaces act as nucleation sites for nanostructure growth and facilitate the formation of metal NPs. In particular, the metal ions could be adsorbed on the GO nanosheets by the coordination with the functional moieties on GO. Under the reduction atmosphere provided by sodium citrate or/and ascorbic acid at elevated temperature, the metal ions are reduced to crystals and deposited on the GO surfaces. Given the possible Ostwald ripening effect and aggregation of small particles, particularly NPs, controlling the size and improving the homogeneous distribution of noble metal NPs are important. The sodium citrate reduction system was employed in the synthesis of Au and Pt NPs on GO, in which sodium citrate acts as a mild reductant and stabilizer for the kinetically controlled synthesis of Au and Pt. However, sodium citrate did not work well for the case of Pd, and thus another reductant (ascorbic acid) was added to the reduced system to produce Pd NPs with high crystallinity and narrow size distribution. The experimental results show that the size and distribution of metal NPs can be adjusted by changing the amount of sodium citrate and the ratio between sodium citrate and ascorbic acid. Fig. 1 shows the typical TEM images of the

as-prepared composites. The metal NPs with varying sizes and distributions were uniformly deposited onto the GO surface. The high-resolution TEM (HRTEM) images (Figs. 1d–1f) show that the lattice spacing of the Au, Pt, and Pd NPs are 0.23, 0.23, and 0.24 nm, respectively, corresponding to the distance of the (111) lattice spacing of the metal crystals. The results suggest that Au, Pt, and Pd NPs are successfully attached onto the GO surface. We can also see that the size and distribution of Au NPs (Fig. 1a) is more homogeneous than that of Pt NPs (Fig. 1b) although the identical reduced system used. The size non-homogeneous of Pt NPs compared with Au NPs probably due to the fact that sodium citrate would not be the most suitable reducdant for the preparation of Pt NPs, although it can reduce and protect Au NPs effectively. In addition, the Au NPs are preferentially distributed on the surface of GO, whereas Pt NPs exhibit low surface distribution density. The Pt NPs were found to be anchored at the edges of GO, which are known to be highly defective compared to its surface because of the presence of a large number of dangling bonds and vacancies [13-15]. The starting experimental reaction step of aging the solution containing gold (III) and platinum (IV) irons is proposed to result in the formation nuclear

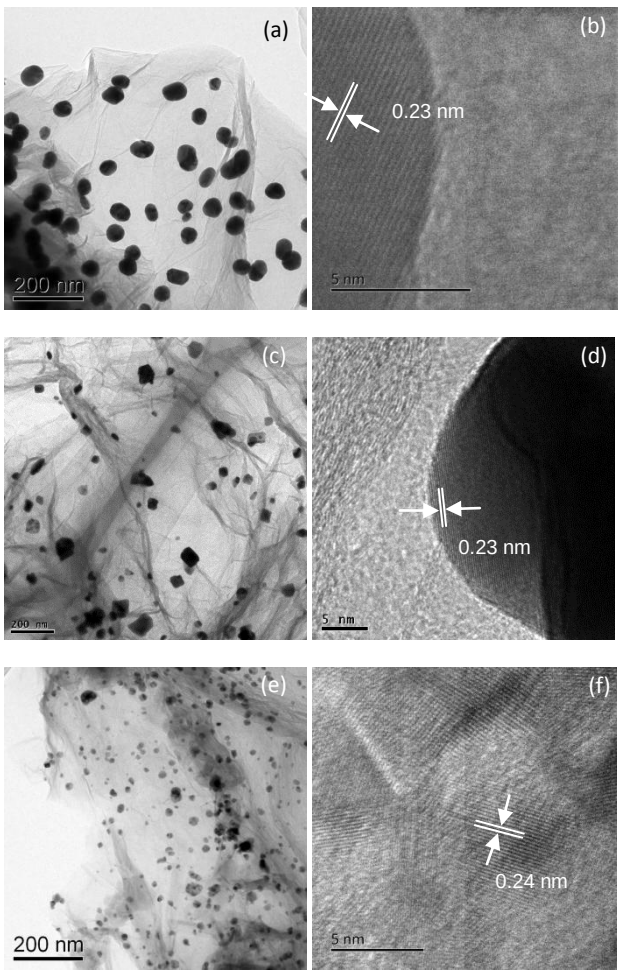

Fig. 1. Typical TEM images of (a) GO/Au-NPs, (b) GO/Pt-NPs, and (c) GO/Pd-NPs; HRTEM images of (d) Au NPs, (e) Pt NPs, and (f) Pd NPs.

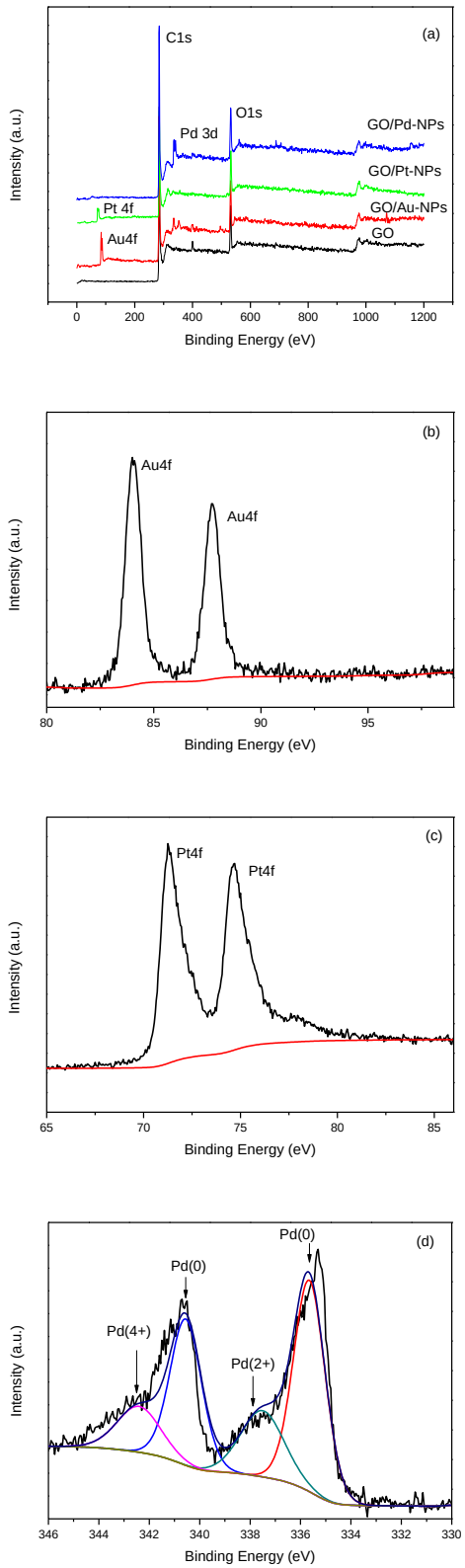

Fig. 2. XPS spectra of (a) GO and GO/metal NP composites, (b) Au 4*f* in GO/Au-NPs, (c) Pt 4*f* in GO/Pt-NPs, and (d) Pd 3*d* in GO/Pd-NPs.

sites of Au NPs in GO surfaces and Pt NPs at GO edges owing to the more active platinum (IV) irons than gold (III) irons. Subsequently, the reduction process enables the growth of Au NPs at the GO surface and Pt NPs at the GO edge, which can explain the differences in distribution of GO/Au-NPs and GO/Pt-NPs.

The formation of GO/metal NP composites was further characterized using XPS, and the survey spectra are presented in Fig. 2(a). Compared with GO, the appearances of the Au 4*f*, Pt 4*f*, and Pd 3*d* signals in the survey scan of GO/Au-NPs, GO/Pt-NPs, and GO/Pd-NPs indicate that Au, Pt, and Pd NPs are successfully assembled onto the GO surface. As shown in Figs. 2(b) and 2(c), two main peaks are observed for GO/Au-NPs and GO/Pt-NPs and no other peak can be deconvoluted. Thus, the hydrothermal reaction reduces the $HAuCl_4$ and H_2PtCl_6 into their metallic states. However, the deconvolution spectrum of the GO/Pd-NPs shows that the peak of the sample mainly contains Pd zero valence state and small positive tetravalent Pd, which possibly originated from the surface oxidation of Pd during synthesis at 100 ℃.

3.2 Structure of the GO/metal NP composites

Raman spectroscopy is a common and effective method in characterizing carbon-based materials and the sp^2 and sp^3 carbon atoms in graphite, diamond, fullerene, carbon nanotubes, graphene, and other carbon materials, as well as in obtaining their structural features. The Raman spectra of GO and GO/metal NP composites are presented in Fig. 3. Two characteristic peaks appeared in the GO within the range of 1000 cm^{-1} to 2000 cm^{-1}, which are named as G band and D band, respectively. The G band centered at 1596 cm^{-1} is assigned to the E_{2g} phonon of C sp^2 atoms, whereas the D band located at 1320 cm^{-1} is a breathing mode of κ-point phonons of A_{1g} symmetry, which originated from the edges, other defects, and disordered carbons. The intensity and location of the G and D bands are unchanged in the three investigated GO/metal NP composites. This finding confirms that the structure of GO are conserved after the reaction with Au, Pt, and Pd NPs, which is mainly due to the formation of the composite structure involving electrostatic interactions and van der Waals forces between the functionalities on the GO surface and those on the monolayer metal NPs. Moreover, the retention of the GO intrinsic structure is important for maintaining the optimal properties of the GO in the composite materials.

3.3 NLO and OL properties of the GO/metal NP composites

In the present study, we applied an OA *Z*-scan technique to investigate the NLO and OL properties of the GO and GO/metal NP composites. Fig. 4 shows the OA *Z*-scan results at 200 μJ incident energy and 532 nm laser wavelength. The sample concentrations were adjusted to obtain a similar linear transmittance of 75% at 532 nm in 1 mm thick cells to compare the NLO effects. In the OA *Z*-scan, the transmittance of the sample is determined during its translation through the focal plane of a tightly focused beam. As the sample moves closer to the focus, the beam intensity increases and the nonlinear effect happens, which then results in a decreasing transmittance because of RSA, TPA, and NLS. The depth of the valley in the *Z*-scan curve directly determines the extent of the NLO performance. Thus, the NLO property is significantly enhanced after metal NP inclusion on the GO surface. As shown in Fig. 4, the GO/Au-NP composite shows the largest dip among the *Z*-scan curves of the studied materials.

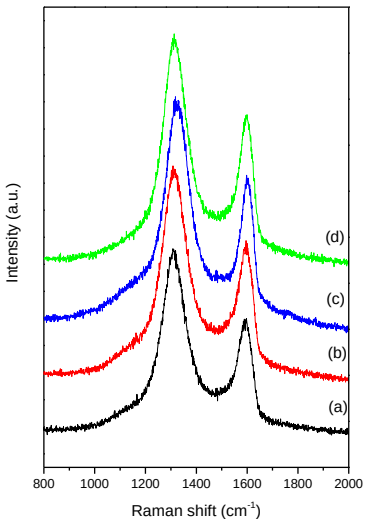

Fig. 3. Raman spectra of (a) GO, (b) GO/Au-NP, (c) GO/Pt-NP, and (d) GO/Pd-NP composites.

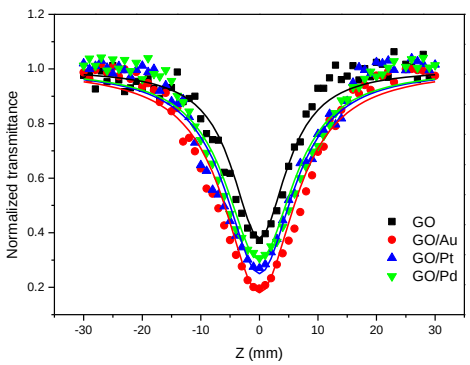

Fig. 4. OA *Z*-scans for GO and GO/metal NPs at 532 nm. The dots correspond to the experimental results, whereas the solid lines represent the best-fit curves based on the *Z*-scan theory.

Therefore, the GO/Au-NP composite demonstrates a better NLO effect than pure GO and GO/Pt-NP and GO/Pd-NP composites.

The measured OA *Z*-scan curves can be fitted numerically to a transmission equation for a third-order nonlinear process provided by: [25]

$$T(z,s=1)=\frac{1}{\sqrt{\pi}q_0(z,0)}\int_{-\infty}^{\infty}\ln\left[1+q_0(z,0)e^{-r^2}\right]dr \quad (1)$$

Where $q_0(z,0)=\beta I_0 L_{eff}$, β is the nonlinear absorption coefficient, I_0 is the on-axis peak intensity at the focus ($z=0$), $L_{eff}=[1-\exp(-\alpha l)]/\alpha$ is the effective thickness of the sample, α is the linear absorption coefficient, and l is the sample thickness. The nonlinear absorption coefficient can be determined by fitting Eq. (1) with the experimental data obtained from the OA *Z*-scan. The β values for the GO and GO/metal NP composites are

extracted from the best-fit curve (Table 1). Table 1 shows that β increases in the following sequence: GO < GO/Pd-NPs < GO/Pt-NPs < GO/Au-NPs. This finding further indicates that the NLO effect of GO can be modified by absorbing different metal NPs on its surface.

The OL curves presented in Fig. 5 were calculated from the corresponding OA *Z*-scan results. The curves demonstrate the variations of the normalized transmittance versus input fluence. At low fluence, the transmittance for the GO/metal NP composites is independent of the input fluence and the values are almost constant until 0.02 J/cm^2. At higher input fluence, the OL effect was observed for all GO/metal NP composites and transmissions drastically decrease to lower than 0.4 at 1.0 J/cm^2. As the input energy increased, the reduction of transmittance versus input fluence was observed. The results reveal that the OL efficiencies of all coated GO samples are significantly higher than that of the GO alone. OL threshold is defined as the input fluence at which transmittance decreases to 50% of the linear transmittance because of nonlinearity. The optimal limiting thresholds of GO, GO/Au-NP, GO/Pt-NP, and GO/Pd-NP composites are at 0.56, 0.32, 0.40, and 0.47 J/cm^2, respectively.

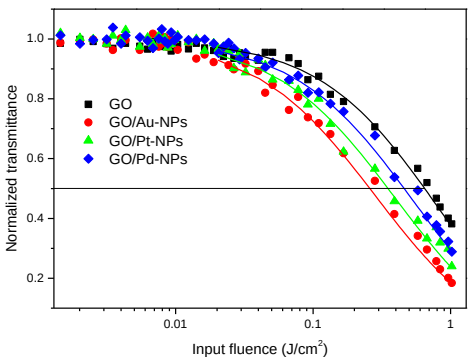

Fig. 5. Normalized transmittance as a function of input fluence.

Table 1. The nonlinear absorption coefficient (β) and OL threshold (F_{th}) for the GO and GO/metal NP composites.

Samples	B (cm/GW)	F_{th}(J/cm^2)
GO	0.83	0.56
GO/Au-NPs	1.1	0.32
GO/Pt-NPs	1.0	0.40
GO/Pd-NPs	0.94	0.47

In general, OL behavior is derived mainly from NLA (2PA, free-carrier absorption, and RSA), nonlinear refraction, and NLS [25]. The mechanisms of NLO and OL behavior in GO have been well studied; such mechanisms mainly originate from RSA [7]. Moreover, considering that the valleys in the OA *Z*-scan curves can be the signature of either NLA or NLS, an experiment involving NLS measurements was performed to determine its contribution to the observed OL effects in the GO nanostructures. The typical NLS results of the GO and GO/metal NP composites are presented in Fig. 6. A significant scattering peak symmetric on the focus is evident in the GO/metal NP composites; such peak indicates NLS. However, no NLS peak for GO was observed, indicating the absence of its contribution. This finding suggests a significant enhancement in NLS caused by the presence of metal NPs in the composites. The key mechanism in NLS is the

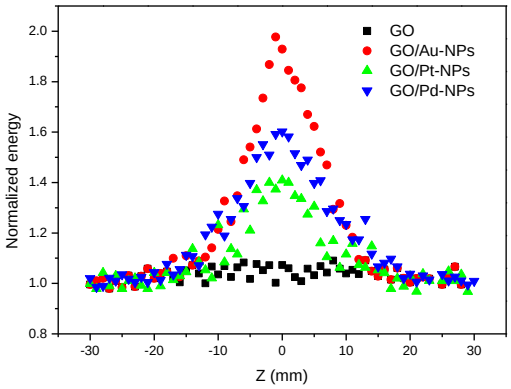

Fig. 6. Typical nonlinear scattering results for GO and GO/metal NP composites at 532 nm. The energy detector is located 45 ° from the axis.

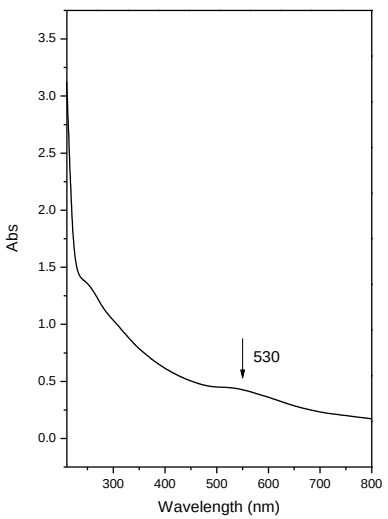

Fig. 7. UV–visible spectrum of GO/Au-NPs.

photon-induced ionization and the excitation of the metal atoms. This mechanism leads to the formation of rapidly expanding microplasma, which strongly scatter the incident light and cause the limiting behavior [26].

Notably, GO/Au-NPs exhibit significantly stronger scattering signal than GO/Pt-NPs and GO/Pd-NPs. We propose that the improvement of NLS in the GO/Au-NPs is mainly due to the SPR in the Au NPs, which is absent in Pt and Pd NPs in the irradiated laser wavelength region. The corresponding bands of this absorption band are located at approximately 530 nm owing to dipolar plasmon mode [27] (as shown in Fig. 7) and are comparable with the excitation laser wavelength employed in the present study; the absorption band is due to the electromagnetic field-induced collective oscillations of the conducted electrons in the states near the Fermi level known as SPR. The relative broadness and weak intensity of this band compared to that of pure Au NPs could be attributed to the inter-particle interactions adsorbed on the surface of the GO, as was previously demonstrated [28]. Specially, the SPR of metal NPs often arises from the transition of the free electrons in the conduction band of metal NPs during a laser pulse excitation. In the course of the intraband transition, the ground-state electrons are pumped to the excited-state. The excited electrons are free carriers possessing a

whole spectrum of energies after the absorption, both kinetic and potential. Once these electrons are excited by a pulse close to absorption peak, they do not oscillate at the same frequency as that of the uncexited electrons, thus causing the ground-state plasmon band to bleach or reduced in intensity [29]. Apart from this, the absorbed photon energy expands the Au NPs into a microplasma state in the sub-nanosecond range and subsequently induces a scattering center. We assumed that the absorbed heat is transferred to the solvent to form microbubbles near boiling temperature. These microplasma and microbubble scattering centers around the metal particles result in a stronger NLS; hence, an enhanced NLO and OL effects in the GO/Au-NPs compared with those of the GO/Pt-NP and GO/Pd-NP composites. Moreover, the GO/Pt-NPs show a slightly stronger NLS than the GO/Pd-NPs because of the relatively large size distribution of Pt NPs. A larger particle can induce larger scattering center and stronger NLS effect. In addition, the presence of small positive tetravalent Pd in the GO/Pd-NPs can also weaken the NLS.

4. Conclusion

In the present study, a series of GO/noble metal (Au, Pt, and Pd) NPs were synthesized via a one-step hydrothermal reaction of $HAuCl_4$, H_2PtCl_6, and $Pd(C_2H_3O_2)_2$ in the presence of GO. The metal NPs with varying sizes and distributions were uniformly deposited onto the GO surface. Moreover, the structure of GO is conserved after loading with Au, Pt, and Pd NPs. The NLO and OL behaviors of the obtained composites were investigated using an OA *Z*-scan technique with nanosecond pulses at 532 nm. The results show that the NLO and OL properties are significantly enhanced after metal NP inclusion onto the GO surface; the improvement depends on the type of the loading metal NPs. The GO/Au-NPs exhibit superior NLO and OL performances among the composite samples. This result can be attributed to the surface plasmon adsorption of Au NPs, in which the corresponding bands are located at approximately 530 nm that is close to the excitation laser wavelength. The NLO and OL effects of GO can be modified by incorporating different metal NPs on its surface. The OL properties in the GO/metal NP composites are attributed to the RSA in the GO sheet and NLS in metal NPs. All of the results indicate that these composites can be used in optoelectronic applications.

Acknowledgments

This work was supported by the National Natural Science Foundation of China (Grant No 61108056).

Notes and references

[a] *College of Materials Science and Engineering, Fujian University of Technology, 3 Xuefu Road, Fuzhou 350118, P. R. China. Fax: 086-591-22863279; Tel: 086-591-22863507; E-mail: czheng.fjut@gmail.com*

1. T. H. Mainan. Nature 1960, 187,493– 494.
2. L.W. Tutt, T.F.A. Boggess. Prog. Quantum Electron. 1993,17,299– 338
3. V. Mamidala, L. Polavarapu, J. Balapanuru, K.P. Loh, Q.H. Xu, and W. Ji. Opt. Express, 2010,18,25928– 25935.
4. C. N. R. Rao, A. K. Sood, K. S. Subrahmanyam, and A. Govindaraj. Angew. Chem. Int. Ed. 2009, 48, 7752 – 7777
5. M. J. Allen, V.C. Tung, and R.B. Kaner. Chem. Rev. 2010, 110, 132–145.
6. O.C. Compton, and S.B.T. Nguyen. Small 2010, 6, 711–723.
7. Z.B. Liu, X.L. Zhang, Y.F. Xu, Y.S. Chen, and J.G. Tian. Appl. Phys. Lett. 2009, 94, 021902.
8. M. Feng, H.B. Zhan, Y. Chen. Appl. Phys. Lett.2010, 96, 033107.
9. N. Liaros, P. Aloukou, A. Kolokithas-Ntoukas, A. Bakandritsos, T. Szabo, R. Zboril, and S. Couris. J. Phys. Chem. C 2013, 117, 6842–6850.
10.X.Q. Zheng, M. Feng, H.B. Zhan. J. Mater. Chem. C 2013, 1, 6759–6766.
11. L.L. Tao, B. Zhou, G.X. Bai, Y.G. Wang, S.F. Yu, S.P. Lau, Y.H. Tsang, J.Q. Yao, and D.G. Xu. J. Phys. Chem. C 2013, 117, 23108–23116.
12. X.-F. Jiang, L. Polavarapu, S.T. Neo, T. Venkatesan, Q.H. Xu. J. Phys. Chem. Lett. 2012, 3, 785–790.
13. D. Chen, H.B. Feng, and J.H. Li. Chem. Rev. 2012, 112, 6027−6053.
14. K. P. Loh, Q. L. Bao, P. K. Ang and J. X. Yang. J. Mater. Chem. 2010, 20, 2277–2289
15. V. Georgakilas, M. Otyepka, A.B. Bourlinos, V. Chandra, K. Namdong, K.C. Kemp. Chem. Rev. 2012, 112, 6156–214.
16. J.H. Zhu, Y.X. Li, Y. Chen, J. Wang, B. Zhang, J.J. Zhang, and W. J. Blau. Carbon 2011, 49, 1900-1905.
17. M. Feng, H.B. Zhan, Y. Chen. Nanotechnology 2010, 21, 075601.
18. Y.F. Xu, Z.B. Liu, X.L. Zhang, Y. Wang, J.G. Tian, Y. Huang, Y.F. Ma, X.Y. Zhang, and Y.S. Chen. Adv. Mater. 2009, 21, 1275–1279.
19. B. Anand, A. Kaniyoor, S.S.S. Sai, R.J. Philip, S. Ramaprabhu. J. Mater. Chem. C 2013, 1, 2773–80.
20. Z.Y. Sun, N.N. Dong, K.P. Wang, D.N. Kőnig, T.C. Nagaiah, M.D. Sánchez. Carbon 2013, 62, 182–192.
21. M.Y. Han, W. Huang, C.H. Chew, L.M. Gan, X.J. Zhang, and W. Ji. J. Phys. Chem. B 1998, 102, 1884.
22. P.V. Kamat, M. Flumiani, G.V. Hartland, J. Phys. Chem. B 1998, 102, 3123.
23. L. Francois, M. Mostafavi, J. Belloni, J. Delouis, J. Delaire, P. Feneyrou, J. Phys. Chem. B 2000, 104, 6133.
24. W.S. Hummers, and R.E. Offeman. J. Am. Chem. Soc. 1958, 80, 1339.
25. M. Sheik-Bahae, A.A. Said, T.-H. Wei, D.J. Hagan, and E.W.V. Stryland. IEEE J Quantum Electron 1990, 26, 760–769.
26. H. Pan, W.Z. Chen, Y.P. Feng, W. Ji. Appl.Phys. Lett. 2006, 88,223106
27. Y.H. Lee, L. Polavarapu, N.Y. Gao, P.Y. Yuan, Q.-H. Xu. Langmuir 2012, 28, 321–326.
28. M.A. Correa-Duarte, L.M. Liz-Marzán, M. Giersig. Adv. Mater. 2004, 16, 2179–2184.
29. S.L. Qu, Y.C. Gao, X.W. Jiang, H.D. Zeng, Y.L. Song, J.R. Qiu, et al. Opt. Commun. 2003, 224, 321–327.